2020 IEEE/RSJ International Conference on Intelligent Robots and Systems (IROS)
October 25-29, 2020, Las Vegas, NV, USA (Virtual)

Tumbling and Hopping Locomotion Control for a Minor Body Exploration Robot

Keita Kobashi[1], Ayumu Bando[1], Kenji Nagaoka[2], and Kazuya Yoshida[1]

Abstract— **This paper presents the modeling and analysis of a novel moving mechanism "tumbling" for asteroid exploration. The system actuation is provided by an internal motor and torque wheel; elastic spring-mounted spikes are attached to the perimeter of a circular-shaped robot, protruding normal to the surface and distributed uniformly. Compared with the conventional motion mechanisms, this simple layout enhances the capability of the robot to traverse a diverse microgravity environment. Technical challenges involved in conventional moving mechanisms, such as uncertainty of moving direction and inability to traverse uneven asteroid surfaces, can now be solved. A tumbling locomotion approach demonstrates two beneficial characteristics in this environment. First, tumbling locomotion maintains contact between the rover spikes and the ground. This enables the robot to continually apply control adjustments to realize precise and controlled motion. Second, owing to the nature of the mechanical interaction of the spikes and potential uneven surface protrusions, the robot can traverse uneven surfaces. In this paper, we present the dynamics modeling of the robot and analyze the motion of the robot experimentally and via numerical simulations. The results of this study help establish a moving strategy to approach the desired locations on asteroid surfaces.**

I. Introduction

The exploration of asteroids is an interesting and scientifically lucrative endeavor owing to the wealth of information asteroids may contain about the origin and evolution of our solar system. The gravitational acceleration of asteroids has been estimated to be between 1.0×10^{-5} m/s^2 and 1.0×10^{-2} m/s^2. Owing to the microgravity environment on asteroid surfaces, friction-based locomotion such as wheel mobility, which significantly depends on gravity, cannot achieve sufficient locomotion [1]. Moreover, robots utilizing such locomotion are likely to experience significant bumps and ground reaction forces resulting in periods of unintentional floating. [2].

To overcome friction-based locomotion limitations, several moving mechanisms have been invented for adapting to the microgravity environment; examples include hopping mobility and the ciliary vibration drive [3] – [5]. A sampling of hopping and ciliary locomotion robots includes MINERVA, MASCOT, and MINERVA-II as developed by Japan Aerospace Exploration Agency (JAXA) and Centre National d'etudes Spatiales (CNES), and JAXA, respectively. However, the conventional mechanisms have vital problems to access the desired locations on asteroid surfaces. Therefore, these problems should be addressed for the success of future missions.

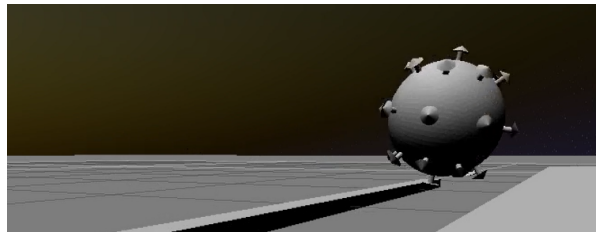

Fig. 1. 3D Image of Our Robot

Hopping mobility is induced by an impulsive force that is derived from robots' internal actuator. Various actuators have been explored in previous studies, such as motors with a flywheel [6], elastic energy derived from internal springs [7], and the deformation of a bimetal exposed to a temperature gradient [8]. Although the effectiveness of the hopping mobility was demonstrated by MINERVA-II during the landing on the surface of Ryugu, the robots utilizing this hopping mobility may experience repeatedly rebound on asteroid surfaces and lose their moving directivity. While some space probes have observed the surfaces of asteroids [9] and [10], the characteristics of asteroids' surfaces are varied, and hence, further investigation is required. Consequently, for practical use, the soft-landing techniques for such hopping rovers that can adapt to unknown asteroid surfaces, are still difficult to achieve. Hence, such hopping rovers cannot explore their desired locations.

Alternatively, ciliary vibration-type motion is generated by the oscillation of the robot [11] – [13]. For ciliary-type motion robots, elastic bodies attached to the body of the robot are bend, and the elastic forces generated from the transformation of its cilia work as the propulsion forces. Owing to this mobility, the motion is predictable [14]; however, most of the sequence of this mobility is crawling on the ground. Therefore, ciliary-type motion robots experience great difficulty of traversing uneven surfaces, even if the obstacles are small.

Moreover, legged robots utilizing their limb to grasp boulders on asteroid surfaces have been invented by the National Aeronautics and Space Administration (NASA) [15]. This mechanism overcomes the challenges of the moving directivity and the traversability. However, such robots have

[1] Keita Kobashi, Ayumu Bando, and Kazuya Yoshida with Department of Aerospace Engineering, Graduate School of Engineering, Tohoku University, Sendai, 980-8579, Japan {kobashi, yoshida}@astro.mech.tohoku.ac.jp

[2] Kenji Nagaoka with Department of Mechanical and Control Engineering, Graduate School of Engineering, Kyushu Institute of Technology, Kitakyushu, 804-8550, Japan nagaoka.kenji572@mail.kyutech.jp

complex systems that require intricate controllers. Therefore, the practical use of legged robots in real missions is still affected by various obstacles.

In contrast to asteroid exploration, the proposed tumbling locomotion exhibits advantages in overcoming these significant challenges. Tumbling locomotion is induced by an internal actuator and the spring-mounted spikes attached to the perimeter of the robot. The reaction torque generated by the internal actuator makes the robot rotate, and the contacts between the spikes and the ground have the spikes transform. Thus, the robot obtains its motion through the frictional and elastic forces of the spikes interacting with the ground.

During tumbling, the robot maintains contact with the ground; thus, contributing to the controllability of the robot and consequently, the predictability of the robot's motion. Moreover, the tumbling locomotion enables the robot to traverse uneven surfaces because the spikes are able to grapple steps and small obstacles on asteroid surfaces. Accordingly, the tumbling motion improves the chances of the robot approaching its desired locations and expands the scope of its action on asteroid surfaces.

In this paper, we mention the dynamics modeling of the small tumbling robot and analyze the characteristics of the tumbling motion based on numerical simulations. Moreover, some physical experiments are conducted to validate the proposed dynamics model.

II. Locomotion Mechanism

In this section, we address the mechanism of the proposed tumbling locomotion. The notions of conventional hopping and ciliary vibration drive are described in Fig. 2 (a) and Fig. 2 (b). As shown in Fig. 2 (a), the internal actuator of the robot realizes the hopping mobility. Robots utilizing this mobility have a significant drawback that the robots lose their moving directivity because of the repeated rebounding. Conversely, the ciliary vibration drive described in Fig. 2 (b) has high directivity. While traversing asteroid surfaces, the robots assuming ciliary vibration driving mobility have high chances to touch the ground because of the micro-hopping, which enables them to have high moving directivity. However, the robots cannot traverse uneven surfaces by assuming this moving mode.

On the contrary, the proposed moving mechanism, tumbling, can overcome these drawbacks involved in the conventional mobilities while holding the advantages of these two moving modes. Moreover, the tumbling movement can be generated by an internal torque, which can also generate the hopping movement. Therefore, robots utilizing the tumbling mobility are able to switch two moving modes using an actuator.

The sequence of motion is shown in Fig. 3. The robot receives the reaction torque derived from the rotation of its internal motor. Based on the magnitude of the reaction torque, the robot selects one of the two moving modes, tumbling and hopping.

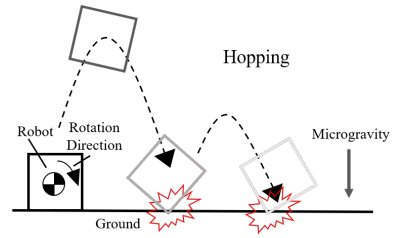

(a) Hopping

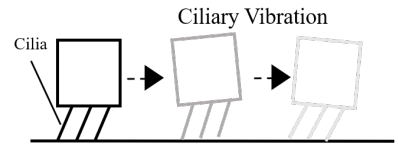

(b) Ciliary Vibration

Fig. 2. Notions of Conventional Movement

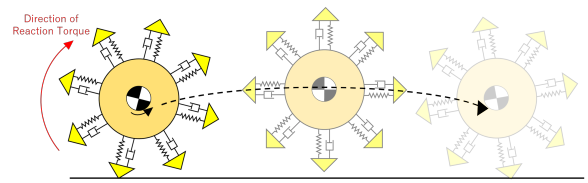

Fig. 3. Tumbling Mechanism

III. Definition of Tumbling and Hopping

For clarity, we define the two significant modes of the robot's motion, tumbling and hopping.

- Tumbling: As shown in Fig, 4 (a), the spikes of the robot contact the ground, sequentially. Periods of no contact with the ground are possible; however, less than a revolution in the air is required.
- Hopping: As shown in Fig. 4 (b), contact is not maintained with the ground. The spikes of the robot are not required to contact the ground sequentially. A single revolution or more is necessary while floating in the air.

IV. Dynamics Modeling

In this study, we address the robot in a 2D environment. The robot exhibits a circular shape and has eight spikes connected by linear springs and dampers. The internal actuator is located at the geometric center of the robot.

A. Equation of Motion

From Fig. 5, when one of the robot spikes is in contact with the ground surfaces, the forces obtained using the

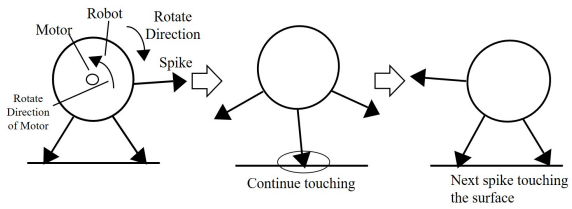

(a) Tumbling

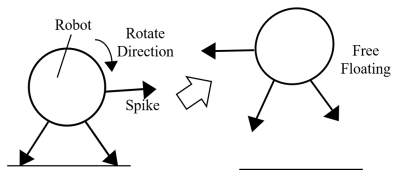

(b) Hopping

Fig. 4. Definition of Motion

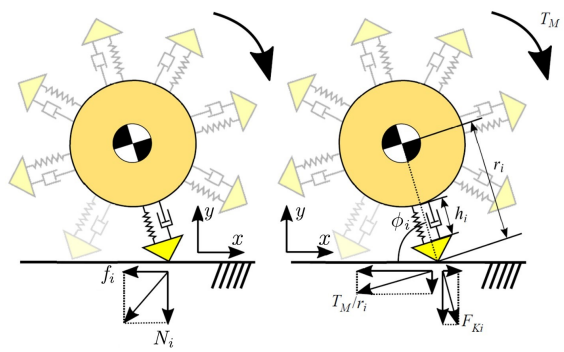

Fig. 5. Reaction Forces

following equations act on the robot.

$$m\frac{d^2x}{dt^2} = \sum_{i=1}^{n} f_i \tag{1}$$

$$m\frac{d^2y}{dt^2} = mg + \sum_{i=1}^{n} N_i \tag{2}$$

$$I\frac{d^2\theta}{dt^2} = \sum_{i=1}^{n} N_i r\cos\phi - \sum_{i=1}^{n} f_i r_i \sin\phi + T_M \tag{3}$$

Since the spikes are connected by linear springs and dampers, N_i and f_i are described as follows:

$$N_i = \frac{T_M}{r_i}\cos\phi + F_{K_i}\sin\phi \tag{4}$$

$$f_i = \begin{cases} \frac{T_M}{r_i}\sin\phi - F_{K_i}\cos\phi & \text{(Static Friction)} \\ \mathrm{sgn}(v_{x_i})\mu N_i & \text{(Maximum Static Friction)} \\ \mathrm{sgn}(v_{x_i})\mu_d N_i & \text{(Dynamic Friction)} \end{cases} \tag{5}$$

$$F_{K_i} = k(h_0 - h) - d\frac{dh}{dt} \tag{6}$$

B. Motor Equation

The robot adopts a DC motor as its internal actuator. The centrifugal force produced by an eccentric motor can be expressed as follows:

$$\begin{cases} F_{Mx} = m_e r_e \left(\frac{d\theta_M}{dt}\right)^2 \cos(\theta_M + \theta) \\ F_{My} = m_e r_e \left(\frac{d\theta_M}{dt}\right)^2 \sin(\theta_M + \theta) \end{cases} \tag{7}$$

Moreover, we discuss the centrifugal torque derived from the DC motor. This robot system has a brushed DC motor that rotates the eccentric masses. Generally, the equations of a DC motor can be expressed as follows:

$$T_M = K_T I_M = J_M \frac{d^2\theta_M}{dt^2} + \nu_M \frac{d\theta_M}{dt} + T_r \tag{8}$$

$$V_M = L_M \frac{dI_M}{dt} + R_M I_M + K_E \frac{d\theta_M}{dt} \tag{9}$$

In the case that the motor does not have a gear head, ν_M is ideally equal to 0. In addition, since the center of gravity of the eccentric masses is not collocated with the rotation axis of the motor, the following disturbing torque affects the motor.

$$T_r = -m_e r_e \cos(\theta_M + \theta) \tag{10}$$

However, in this case, T_r is virtually equal to 0 because g is significantly smaller than 1 owing to the microgravity environment.

Moreover, we assume $V_M \approx R_M I_M + K_E \frac{d\theta_M}{dt}$ in the subsequent analysis model since an electrical time constant of a motor L_M/R_M is significantly smaller than a mechanical time constant. For these approximations, $\frac{d^2\theta_M}{dt^2}$ and T_M are

Variables	Name
m	Total mass of the robot
I	Moment of inertia of the robot
i	Spike indice
n	Number of spikes contacting surface
f_i	Frictional force acting on ith spike
N_i	Normal force acting on ith spike
T_M	Centrifugal torque of the motor
x	Horizontal position of the robot
y	Vertical position of the robot
θ	Attitude of the robot
r_i	Rotational radius
ϕ_i	Angle between ith spike

TABLE I

VARIABLES IN EQUATIONS (1)–(3)

Variables	Name
F_{K_i}	Elastic-damping force of the ith spike
v_{x_i}	Horizontal portion of translational velocity of the ith spike
μ	Static friction coefficient
μ_d	Dynamic friction coefficient

TABLE II

VARIABLES IN EQUATIONS (4)–(6)

described as follows:

$$\frac{d^2\theta_M}{dt^2} = \frac{K_T}{J_M R_M}\left(V_M - K_E \frac{d\theta_M}{dt}\right) \tag{11}$$

$$T_M = \frac{K_T}{R_M}\left(V_M - K_E \frac{d\theta_M}{dt}\right) \tag{12}$$

T_M is the exerted torque from the motor, hence the robot receives T_M as its reaction torque.

V. Numerical Simulation

In this section, we discuss the numerical simulations conducted to evaluate the characteristics of the tumbling and hopping motions. The dynamics model discussed in Section IV is used in these simulations. Parameters of the robot used in these simulations are listed in Table V. Here, r_{body} and l_{spike} denote the radius of the body and the length of a spike, respectively.

A. Tumbling Characteristics

1) Analysis of Translational Velocity: To begin with, we analyze the translational velocity of the robot during tumbling. We assume a flat surface and assign T_M in the range between 0.01 N·m and 0.015 N·m until the end of the simulation. In this simulation, we set g $2.5 \times 10^{-3}\text{m/s}^2$.

The x and y portions of translational velocity v_x and v_y are shown in Fig. 6 (a) – (f). In these figures, the profiles of the velocity appear as almost two piecewise linear lines. The slope of the linear line indicates the acceleration of the robot. We assign α_1 and α_2 as the representatives of these acceleration, which $\alpha_1 > \alpha_2$. When the spikes of the robot receive static frictional forces, the acceleration is equal to α_1; conversely, when the spikes receive dynamic frictional forces, the acceleration of the robot is α_2. Hence, the acceleration of the robot appears to experience one significant discrete change, while tumbling and the friction coefficient changes at this discrete change. As mentioned in Section IV, the static and dynamic frictional forces are $T_M/r\sin\phi - F_{K_i}\cos\phi$ (Static Friction) and $T_M/r\cos\phi + F_{K_i}\sin\phi$, respectively. Generally, the static friction forces are larger than the dynamic friction forces; therefore, α_1 corresponds to the static friction forces and α_2 corresponds to the dynamic friction forces. The friction forces depend on T_M. Thus, the large torque T_M enlarges α_1 and α_2. However, α_1 and α_2 are not proportional to T_M since the energy that the robot receives from T_M are partially converted to the vertical component of the robot's momentum.

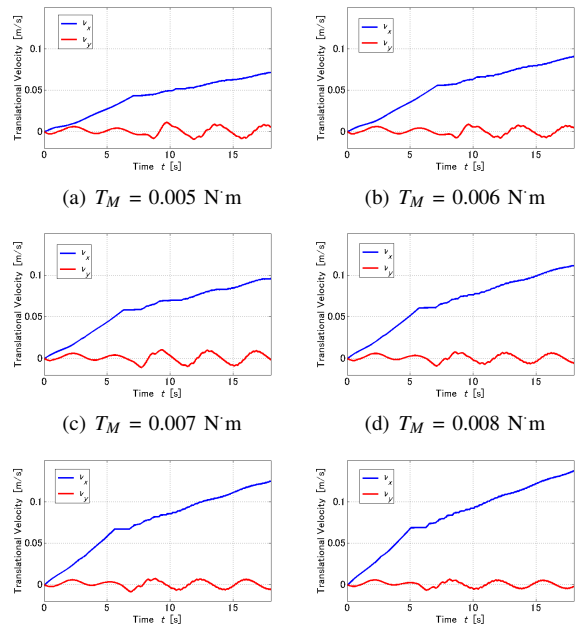

(a) T_M = 0.005 N·m (b) T_M = 0.006 N·m (c) T_M = 0.007 N·m (d) T_M = 0.008 N·m (e) T_M = 0.009 N·m (f) T_M = 0.01 N·m

Fig. 6. Time Profile of Tumbling Velocity

2) Climbing Ability: To evaluate the traversability on uneven asteroid surfaces with the tumbling motion, analyzing the ability to climb a step plays a key role. We assume the initial state of the robot as one of its spikes is on the ground and the other is about to locate on a step. Using this simulation, we evaluate the ability of the robot to climb a step. The result of this simulation is represented in Table. VI. In these simulations, we set g 2.5×10^{-3} m/s^2 and T_M 0.015 N·m until the end of simulation. However, g and T_M are irrelevant to the climbing ability. Even if g is large, the

Variables	Name
m_e	Eccentric mass
r_e	Effective radius between the rotational axis and the center of gravity of an eccentric mass
θ_M	Rotation angle of the motor

TABLE III

Variables in Equations (7)

Variables	Name
J_M	Sum of the moment of inertia including all eccentric masses
ν_M	Motor's damping coefficient
T_r	Disturbing torque
K_T	Motor's torque constant
I_M	Motor's current
L_M	Inductance of the motor
R_M	Inner resistance of the motor
K_E	Inverse electromotive force constant
V_M	Input voltage

TABLE IV

Variables in Equations (8)–(9)

Parameters	Value
m	4.45 kg
I	0.0154 kgm^2
m_e	0.0012 kg
μ	2.25
μ_d	1.8
k	15 N/m
d	0.3 Ns/m
h_0	0.015 m
r_{body}	0.10607 m
l_{spike}	0.015 m

TABLE V

Parameters for Numerical Simulation

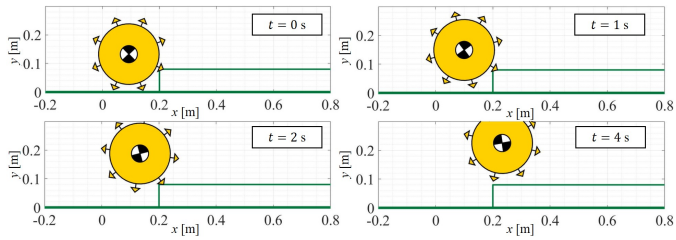

(a) Success Case (0.08 m)

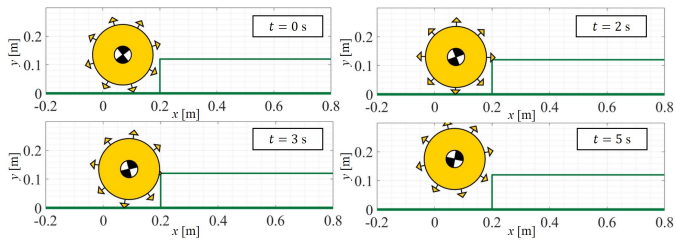

(b) Failure Case (0.12 m)

Fig. 7. Climbing Simulation

robot can climb by receiving the large T_M. This result shows that the threshold is located between the heights of 0.10 m and 0.12 m. When the spike of the robot is on top of the step, then the robot has finally climbed the step. However, when no spike is on the step, one of the spikes initially touches the lateral side of the step. This contact occurs when the robot and its repulsive force are not into contacts with the step. Therefore, the threshold can be determined by the sum of the radius of the body and spike length of the robot because this length determines whether the spike is on the step or not.

B. Switch Tumbling and Hopping

Although the tumbling motion enables the robot to approach the desired locations accurately, some large obstacles on asteroid surfaces can inhibit its movement owing to the limitation of the climbing ability. Hence, the robot should achieve the hopping motion to leap over obstacles, and we have to assess the condition for switching the tumbling and hopping motion. Two conditions are considered for switching these modes.

1) The spike touching the ground must maintain contact with the ground until ϕ exceeds 90°.
2) To maintain static friction, the torque T_M should be below $\mu r F_{K_i}$.

First, we deal with the first condition. If the spike ceases a contact with the ground before ϕ_i reaches 90°, the robot starts floating and stops the tumbling motion. Therefore, the

	Height of Step [m]					
	0.02	0.04	0.06	0.08	0.10	0.12
Ability to Climb	✓	✓	✓	✓	✓	

TABLE VI
RESULTS OF CLIMBING SIMULATION

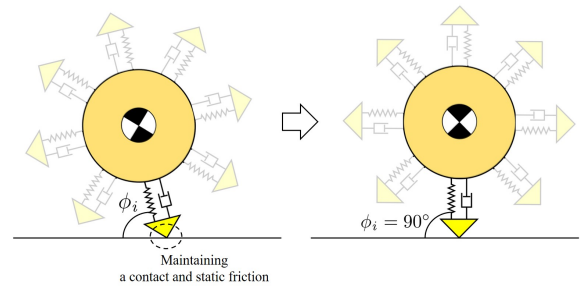

Fig. 8. Conditions of Switching Conditions

spike must maintain the contact with the ground until ϕ_i reaches 90°. To meet this requirement, the natural frequency ($f_{\text{natural}} = \sqrt{k/m}$) of the robot should be low. When the length of the springs attached to the spikes exceeds the original length, the springs start shrinking. This makes the robot to commence floating. Hence, m should be large to prevent the robot from floating. In particular, when g is below 10^{-5}m/s^2 order, the amplitude of vibration extends compared to 10^{-3}m/s^2 or larger case. Consequently, the importance of the heavy mass of the robot increases especially in a low gravity environment.

Second, we address the second condition. In this discussion, the robot must be under the first condition. If the spike touching the ground slips before ϕ_i reaches 90°, the robot starts floating in the air. Hence, the spike of the robot must maintain the static friction until ϕ_i reaches 90°. To maintain the static friction, the horizontal component of the robot's pushing force should satisfy the following equation.

$$f_i < \mu N_i \tag{13}$$

$$\text{i.e. } \frac{T_M}{r}\sin\phi - F_{K_i}\cos\phi < \mu\left(\frac{T_M}{r}\cos\phi + F_{K_i}\sin\phi\right) \tag{14}$$

This equation claims that the horizontal component of its pushing force should be below the maximum static friction force. We can control the torque actively and it mostly affects the horizontal component of its pushing force when ϕ becomes 90°. Therefore, we can obtain the following condition by substituting $\phi = 90°$.

$$T_M < \mu r F_{K_i} \tag{15}$$

VI. EXPERIMENTS

To verify the dynamics modeling proposed in Section IV, we conduct some experiments. The experiment environment and the test bed are shown in Fig. 9 (a) and (b), respectively. This test bed comprises electric circuits with a power battery, an air tank, a brushed DC motor with an eccentric mass, air bearings attached to the bottom of the test bed, and eight spikes made from acrylonitrile-butadiene-styrene (ABS) polymer. Owing to the compressed air in its air tank and the flowing of air from the bottom air bearings, the test bed can float on the granite table. This enables the robot to move in a two-dimensional emulated

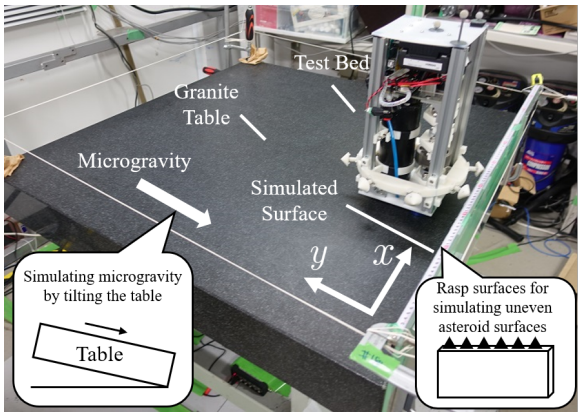

(a) Experiment Environment

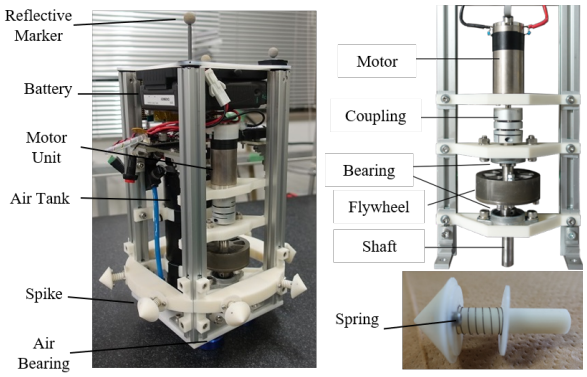

(b) Test Bed

Fig. 9. Overview of the Microgravity Simulating Experiment Environment and Test Bed

microgravity environment. The DC motor is attached to the test bed perpendicularly to the granite table. The weight of this test bed is 4.45 kg. The DC motor is controlled remotely via XBEE, wireless communication modules. The rotational speed of the motor is controlled by a proportional-integral-differential (PID) controller that is implemented on Arduino, a micro controller. The position of the test bed is recorded by an opti-track, motion capture cameras. The acceleration of gravity is generated by slightly tilting the granite table. On the surface that the robot moves, sand paper on a steel plate is attached. This sand paper contributes to simulating the friction coefficient of uneven asteroid surfaces.

A. Tumbling Locomotion

First, we verify the feasibility of the tumbling locomotion. Fig. 10 shows the tumbling locomotion. Fig. 10 indicates that the proposed method actually works in a microgravity environment and its spikes can keep its contact with the simulated surface while tumbling.

Subsequently, to confirm the dynamics model, we apply the motor's torque listed in Table. VII to the robot for 3 s (owing to the specification of the motor) and analyze the tumbling motion. In Table. VII, f_{target} and $\dot{\omega}$ denote the target motor frequency and the angular acceleration of the motor, respectively. In this experiment, we arrange g $2.5 \times 10^{-3}\text{m/s}^2$. Fig. 11 (a) shows the x position of the robot

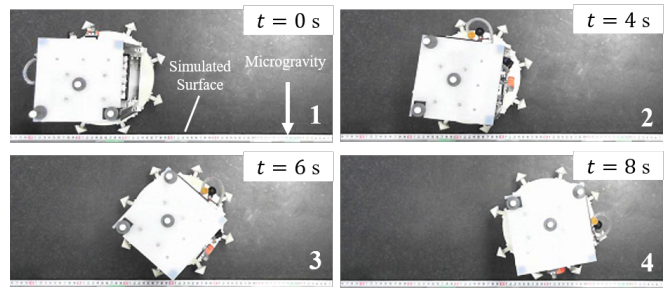

Fig. 10. Sequence of Tumbling Locomotion

in experiments and numerical simulations. Moreover, Fig. 11 (b) shows the x component of the translational velocity of the robot in experiments and numerical simulations. This figure indicates the validity of the dynamics model mentioned in Section IV. Moreover, the translational velocity of the robot increases as the torque proliferates, and the friction status affects the acceleration of the robot. Owing to the applying time of 3 seconds, the velocity decreases suddenly approximately 4 or 5 seconds unlike the numerical simulations. Contacts between a spike and the simulated surface cause the sudden reduction since the contacts disperse the energy of the robot.

B. Climbing Ability

Finally, we verify the robot's ability to climb a step. In this experiment, we prepare two steps whose heights are 0.1 m and 0.12 m, respectively. Based on the limitation of the motor, we apply $T_M = 0.015$ N·m to the robot for 3 seconds. g is $2.5 \times 10^{-3}\text{m/s}^2$.

To begin with, we mention the success case of climbing a step. In this case, the height of the step is 0.1 m, which is approximately equal to the sum of the radius of the body and spike length. Fig. 12 (a) shows the sequence of climbing a step. From these figures, it is obvious that the robot actually climbs a step.

Conversely, in the failure case, the height of the step is 0.12 m, which exceeds the sum of the radius of the body and spike length. Additionally, for the other case, Fig. 12 (b) shows the sequence of climbing a step. From Fig. 12 (b), a spike of the robot has a contact with the lateral surface of the step before the robot completes its climbing motion. The reaction force derived from this contact works as the repulsive force of the robot; therefore, the robot cannot climb the step.

Thus, we can verify that the climbing ability of the robot depends on the sum of the radius of the body and spike

	f_{target} [Hz]	$\dot{\omega}$ [rad/s^2]	T_M [N·m]
#1	20	41.9	0.0100
#2	25	52.4	0.0125
#3	30	62.8	0.0150

TABLE VII
THE TORQUE OF THE MOTOR ASSIGNED FOR ANALYZING TRANSLATIONAL VELOCITY

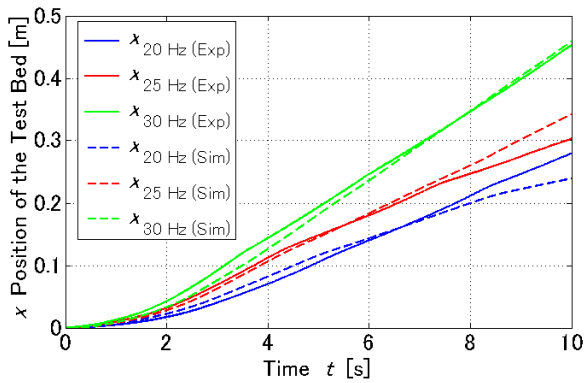

(a) x Position

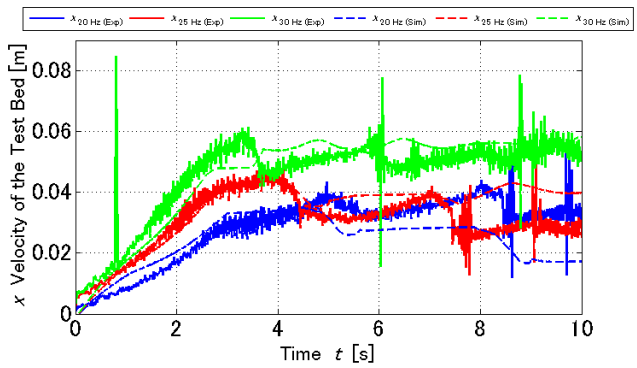

(b) x Velocity

Fig. 11. x Position and Velocity of the Robot while Tumbling

length; specifically, the robot is able to climb only such steps whose height is below the sum.

C. Switch Tumbling and Hopping

Based on the switching condition mentioned in Section IV, we validate the switching conditions of tumbling and hopping modes by experiments. Considering the condition $T_M < \mu r F_{K_i}$, we assign the motor's torque listed in Table. VIII to the robot. At the calculation of T_M, we use F_{K_i} computed from the numerical simulation. In this experiment, we modify g 1.4×10^{-3}m/s^2.

The results of this simulation are described in Fig. 13 (a) and (b). Each of these figures shows the sequences of tumbling and hopping motion of the robot. These figures indicate that the conditions function.

	f_{target} [Hz]	$\dot{\omega}$ [rad/s^2]	T_M [N·m]
#1	20	41.9	0.0100
#2	25	52.4	0.0125

TABLE VIII
THE TORQUE OF THE MOTOR ASSIGNED FOR VALIDATION OF SWITCHING CONDITIONS

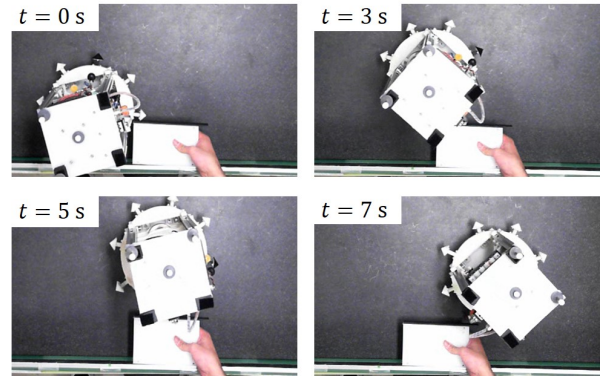

(a) Success Case (0.10 m)

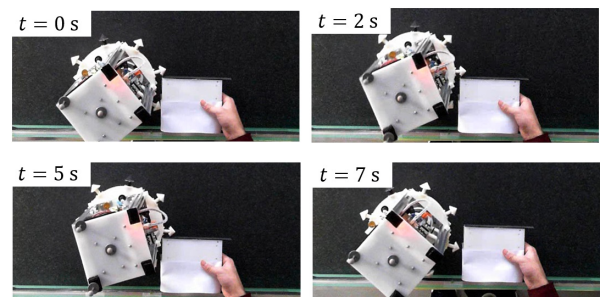

(b) Failure Case (0.12 m)

Fig. 12. Climbing Experiment

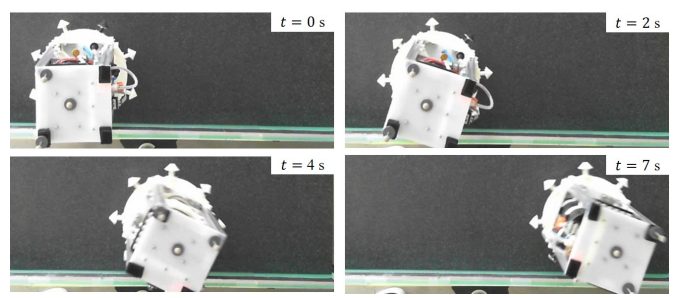

(a) $T_M = 0.0100$ N·m: Tumbling

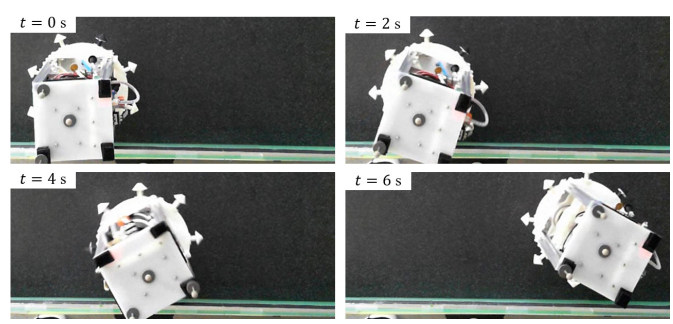

(b) $T_M = 0.0125$ N·m: Hopping

Fig. 13. Switching Tumbling and Hopping

VII. CONCLUSION

In this study, we presented the dynamics modeling and analysis of tumbling locomotion by numerical simulations and physical experiments. The model considers the motor's torque and the elastic damping forces derived from the

spikes. Thus, the robot's motion can be expressed mathematically. Moreover, we analyzed the characteristics of its tumbling motion by numerical simulations. The translational velocity during tumbling locomotion positively depends on the motor's torque, and the robot can climb obstacles whose height is below its radius. In addition, we performed some physical experiments to verify the validity of the dynamics model. These experiments helped validate the proposed dynamics model, and we obtained a deep insight into the characteristics of tumbling locomotion.

For future study, the following two issues should be addressed: One is the mechanical approach, which addresses the effects of the shape of the spikes. The other is the theoretical approach, which deals with the controller to generate the motion of the robot to access the desired locations.

REFERENCES

[1] B. H. Wilcox and R. M. Jones, "The MUSES-CN nanorover mission and related technology," in Proc. 2000 IEEE Aerospace Conf., Big Sky, MT, 2000, vol.7, pp. 287-295.

[2] K. Takahashi, S. Shimoda, K. lizuka and T. Kubota, "A study of locomotion mechanism based on gravitational environment," in Proc. 2004 IEEE/RSJ Int. Conf. Intel. Rob. Syst., Sendai, Japan, 2004, pp. 4001-4006.

[3] T. Yoshimitsu, T. Kubota, I. Nakatani, T. Adachi and H. Saito, "Micro-hopping robot for asteroid exploration" Acta Astronaut., 2003, vol.52, pp. 441-446.

[4] L. Witte, J. Biele, A. Braukhane, F. Herrmann, T. -M. Ho, C. Krause, S. Kuß, C. Lange, M. Schlotterer, S. Ulamee, S. Wagenbach, "The Mobile Asteroid Surface Scout (MASCOT) - System & Mission Engineering and Surface Operations Concept," in Proc. Global Space Exploration Conf. 2012, Washington D.C., 2012.

[5] K. Nagaoka, K. Watanabe, T. Kaneko and K. Yoshida, "Mobility Performance of Ciliary Locomotion for an Asteroid Exploration Robot under Various Experimental Conditions," in Proc. 13th Int. Symp. Artif. Intel., Robot. and Autom. in Space, Beijing, China, S-5a-2, 2016.

[6] T. Yoshimitsu, "Development of autonomous rover for asteroid surface exploration," in Proc. 2004 IEEE Int. Conf. Robot. Autom., New Orleans, LA, 2004, pp. 2529-2534.

[7] S. Shimoda, T. Kubota and I. Nakatani, "New mobility system based on elastic energy under microgravity," in Proc. 2002 IEEE Int. Conf. Robot. and Autom., Washington, DC, 2002, pp. 2296-2301.

[8] Y. Tsumaki, T. Akaike, R. Kazama, T. Mineta and R. Tadakuma, "Environment-Driven Rover for Asteroid Exploration," in Proc. 11th Int. Symp. Artif. Intel., Robot. Autom. in Space, Turin, Italy, P-20, 2012.

[9] H. Yano, T. Kubota, H. Miyamoto, T. Okada, D. Scheeres, Y. Takagi, K. Yoshida, M. Abe, S. Abe, O. Barnouin-Jha, A. Fujiwara, S. Hasegawa, T. Hashimoto, M. Ishiguro, M. Kato, J. Kawaguchi, T. Mukai, J. Saito, S. Sasaki and M. Yoshikawa, "Touchdown of the Hayabusa Spacecraft at the Muses Sea on Itokawa," Science, vol.312, pp. 1350-1353, 2006.

[10] K. Wittmann, B. Feuerbacher, S. Ulamec, H. Rosenbauer, J. P. Bibring, D. Moura, R. Mugnuolo, S. diPippo, K. Szego and G. Haerendel, "Rosetta Lander in situ Characterization of a Comet Nucleus," Acta Astronaut., vol.45, pp. 389-395, 1999.

[11] K. Ioi, "A mobile micro-robot using centrifugal forces," in Proc. 1999 IEEE/ASME Int. Conf. Adv. Intel. Mechatr., Atlanta, GA, 1999, pp. 736-741.

[12] M. Konyo, K. Isaki, K. Hatazaki, S. Tadokoro, and F. Takemura, "Ciliary Vibration Drive Mechanism for Active Scope Cameras," J. Robot. Mechatr., vol.20, pp. 490-499, 2008.

[13] K. Nagaoka, R. Takano, T. Izumo and K. Yoshida, "Ciliary Micro-Hopping Locomotion of an Asteroid Exploration Robot," in Proc. 11th Int. Symp. Artif. Intel., Robot. Autom. in Space, Turin, Italy, 6A-04, 2012.

[14] K. Nagaoka and K. Yoshida, "Modeling and analysis of ciliary micro-hopping locomotion actuated by an eccentric motor in a microgravity," in Proc. 2013 IEEE/RSJ Int. Conf. Intel. Rob. Syst., Tokyo, Japan, 2013, pp. 763-768.

[15] A. Parness, N. Abcouwer, C. Fuller, N. Wiltsie, J. Nash and B. Kennedy, "LEMUR 3: A limbed climbing robot for extreme terrain mobility in space," in Proc. 2017 IEEE Int. Conf. Robot. Autom., Singapore, 2017, pp. 5467-5473.